ChemComm

ROYAL SOCIETY OF CHEMISTRY

COMMUNICATION

View Article Online
View Journal

Cite this: DOI: 10.1039/d6cc01893a

Received 31st March 2026,
Accepted 11th May 2026

DOI: 10.1039/d6cc01893a

rsc.li/chemcomm

Reversing the activity landscape of MoS_x electrocatalysts *via* Ni_xP interfacial coupling for alkaline hydrogen evolution

Ioannis Vamvasakis,*[a] Aggelos Grammenos[b] and Gerasimos S. Armatas *[a]

Interfacial coupling offers a powerful route to modulate electrochemical kinetics, yet its interplay with catalyst morphology remains unclear. Here, Ni_xP coupling reshapes the activity landscape of MoS_x, enabling a highly active amorphous interface for alkaline HER. *Operando* electrochemical analysis reveals a shift beyond Volmer-limited kinetics *via* enhanced charge transfer and hydrogen adsorption.

Green hydrogen production *via* alkaline water electrolysis is central to sustainable energy systems. However, the hydrogen evolution reaction (HER) remains intrinsically sluggish in alkaline media primarily due to the additional energy barrier associated with water dissociation.[1–5] Although Pt-based catalysts exhibit near-optimal HER activity, their scarcity and high cost necessitate the development of efficient earth-abundant alternatives.[6,7] Among these, molybdenum sulfides (MoS_x) have attracted considerable attention owing to their favourable hydrogen adsorption energetics, chemical stability, and structural tunability.[8–14] Nevertheless, their catalytic performance is highly governed by crystallinity and morphology, as active sites are predominantly located at edges and defect-rich domains, while the basal planes are largely inert.[14–17] Consequently, substantial efforts have been devoted to phase engineering,[10,17] nanostructuring,[12,16,17] and defect modulation[18–20] to increase active-site exposure and improve charge-transfer kinetics.

Beyond intrinsic structural optimization, interfacial engineering has emerged as an effective strategy to modulate catalytic activity through electronic coupling between dissimilar phases.[21–25] In this context, nickel phosphides (Ni_xP), particularly amorphous Ni–P phases, are attractive components for hybrid HER catalysts due to their metallic conductivity and favourable hydrogen adsorption energetics.[26–28] Electrodeposition enables precise control over the formation of conformal Ni_xP overlayers on a wide range of sulfide substrates, offering a versatile platform for constructing hybrid electrocatalysts.[29–33] Despite these advantages, the interplay between MoS_x crystallinity and Ni_xP interfacial coupling in governing alkaline HER kinetics remains poorly understood.

Herein, we show that Ni_xP surface modification not only enhances HER activity but fundamentally reshapes the morphology–activity relationship in MoS_x electrocatalysts. Strikingly, Ni_xP coupling inverts the intrinsic activity trend, rendering the amorphous Ni_xP/MoS_x interface the most active configuration. *Operando* electrochemical analysis, combined with kinetic isotope measurements, reveals that interfacial electronic coupling simultaneously accelerates charge-transfer and hydrogen adsorption kinetics, driving a transition beyond the Volmer-limited regime.

Three distinct MoS_x architectures were synthesized on carbon cloth (CC): (i) amorphous electrodeposited MoS_x, (ii) thermally annealed MoS_x at 800 °C (MoS_x-800), exhibiting enhanced crystallinity and preferential base-plane orientation, and (iii) hydrothermally grown MoS_x nanosheets (MoS_x-hydro). Subsequent galvanostatic deposition of amorphous Ni_xP yielded the corresponding Ni_xP/MoS_x, Ni_xP/MoS_x-800, and Ni_xP/MoS_x-hydro heterostructures (Fig. S1). Scanning electron microscopy (SEM) reveals pronounced morphology-dependent differences prior to and following Ni_xP deposition. The electrodeposited MoS_x exhibits a smooth, conformal coating (Fig. S2a–c), whereas MoS_x-800 shows a denser morphology (Fig. S2d–f), consistent with thermally induced densification. In contrast, MoS_x-hydro presents a rough, interconnected nanosheet network (Fig. S2g–i), indicative of an edge-rich structure. After Ni_xP deposition, the overlayer growth is strongly dictated by the underlying MoS_x morphology. On amorphous MoS_x, Ni_xP forms a conformal nanoparticulate overlayer (Fig. 1a), whereas MoS_x-800 yields a dense, featureless Ni_xP layer (Fig. S3a and b), consistent with particle coalescence and limited nucleation heterogeneity. For MoS_x-hydro, the nanosheet architecture is preserved, with Ni_xP nanoparticles uniformly decorating the hierarchical structure (Fig. S3c and d). These observations indicate that Ni_xP nucleation and growth are governed by the

[a] Department of Materials Science and Engineering, University of Crete, Vassilika Vouton, Heraklion 70013, Greece. E-mail: jvamvasakis@uoc.gr, garmatas@uoc.gr
[b] Department of Chemistry, University of Crete, Vassilika Vouton, Heraklion 70013, Greece

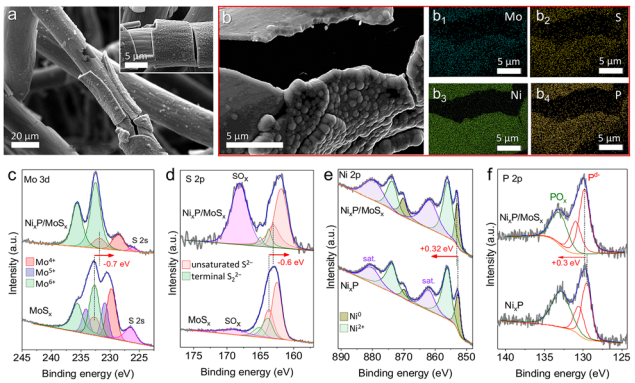

Fig. 1 (a) Representative SEM images of the as-synthesized Ni$_x$P/MoS$_x$. (b) Corresponding EDS elemental mapping showing the spatial distribution of Mo, S, Ni and P. (c) and (d) High-resolution XPS spectra of Mo 3d and S 2p for pristine MoS$_x$ and Ni$_x$P/MoS$_x$. (e) and (f) High-resolution XPS spectra of Ni 2p and P 2p for Ni$_x$P and Ni$_x$P/MoS$_x$.

local surface structure of MoS$_x$, resulting in a morphology-dependent interfacial assembly. Energy dispersive X-ray spectroscopy (EDS, Table S1) shows that electrodeposited MoS$_x$ is slightly sulfur-deficient (Mo : S $\approx$ 1 : 1.4), whereas both MoS$_x$-800 and MoS$_x$-hydro exhibit a stoichiometric MoS$_2$ composition. Upon Ni$_x$P deposition, a Ni-rich surface layer (Ni : P $\approx$ 11–14 : 1) dominates the detected composition, accompanied by attenuation of Mo and S signals due to overlayer screening effects. Notably, the Mo : S ratios remain unchanged relative to the pristine samples, indicating preservation of the underlying MoS$_x$ framework during heterostructure formation. Elemental mapping further corroborates the layered architecture, with Ni and P localized at the surface and Mo and S confined to the substrate (Fig. 1b).

X-ray diffraction (XRD) was employed to assess the crystallinity of the synthesized materials. Electrodeposited MoS$_x$ exhibits no discernible reflections, consistent with an X-ray amorphous structure. In contrast, MoS$_x$-hydro displays broad (002), (100), and (110) reflections characteristic of nanocrystalline 2H-MoS$_2$ (PDF #37-1492; space group: $P6_3/mmc$) (Fig. S4). Notably, MoS$_x$-800 shows a pronounced (002) peak, indicative of enhanced crystallinity and preferential basal-plane orientation parallel to the substrate.[34,35] This structural evolution reflects a transition from a disordered edge-rich structure to a more ordered basal-plane-dominated configuration. Following Ni$_x$P deposition, all heterostructures exhibit a broad diffraction feature at $2\theta \approx 44^\circ$ (Fig. S5), which is characteristic of a quasi-amorphous Ni$_x$P phase. In contrast, Ni-only control samples display sharp reflections corresponding to crystalline metallic Ni, confirming that phosphorous incorporation induces amorphization into a Ni–P phase. Raman spectroscopy provides complementary insight into the local structure. All pristine MoS$_x$ samples exhibit the characteristic in-plane E^1_{2g} and out-of-plane A_{1g} modes of MoS$_2$ at $\sim$383 and $\sim$407 cm^{-1}, respectively (Fig. S6). Among them, MoS$_x$-800 shows sharper and more intense features, consistent with increased crystallinity, whereas MoS$_x$ and MoS$_x$-hydro display broader bands indicative of structural disorder and reduced domain size. Notably, enhanced low-wavenumber modes (145–240 cm^{-1}) are observed for MoS$_x$ and MoS$_x$-hydro, which are attributed to edge-rich or defective MoS$_2$ domains,[36–38] in agreement with XRD. After Ni$_x$P deposition, all heterostructures show broadened Raman peaks (Fig. S7), consistent with disordered metal–metalloid bonding in amorphous Ni$_x$P.[39,40] In contrast, Ni-only control samples display distinct Ni–O vibrational modes that are absent in Ni$_x$P-containing samples, indicating improved resistance of the Ni$_x$P overlayer to surface oxidation.

X-ray photoelectron spectroscopy (XPS) was conducted to probe the chemical states and interfacial electronic interactions. The Mo 3d spectrum of pristine MoS$_x$ can be deconvoluted into Mo^{4+}, Mo^{5+} and Mo^{6+} components (Fig. 1c), where Mo^{5+} species are associated with sulfur vacancies and non-stoichiometric environments characteristic of defective MoS$_x$.[41] Upon Ni$_x$P deposition, the Mo^{5+} contribution is markedly suppressed, leaving predominantly Mo^{4+} and Mo^{6+} states. This evolution indicates a modification of the local electronic structure, arising from interfacial charge redistribution between Ni$_x$P and MoS$_x$. The S 2p spectra comprise contributions from unsaturated S^{2-} and terminal S_2^{2-} species,[42] along with minor SO$_x$ components arising from inevitable surface oxidation (Fig. 1d). The Ni 2p and P 2p spectra confirm the formation of a semi-metallic Ni–P phase composed of metallic Ni and low-valent P$^{\delta-}$ species, with minor oxidized surface contributions (Fig. 1e and f). Importantly, systematic binding energy shifts are observed upon heterostructure formation. The Mo 3d and S 2p peaks shift to lower binding energies ($\sim$0.6–0.7 eV), whereas the Ni 2p and P 2p peaks shift to higher binding energies ($\sim$0.3 eV) relative to their respective references (pure MoS$_x$ and Ni$_x$P). This opposite shift indicates electron transfer from Ni$_x$P to MoS$_x$, providing clear evidence of strong interfacial electronic coupling. Such charge redistribution is expected to optimize hydrogen adsorption energetics and facilitate interfacial charge transfer during the HER. Full XPS peak assignments are summarized in Table S2.

The HER performance of the as-prepared electrodes was evaluated in 1.0 M KOH using a standard three-electrode configuration. Linear sweep voltammetry (LSV) was employed to determine the iR-corrected overpotentials at -10 and -100 mA cm^{-2} (η_{10} and η_{100}), which serve as key activity benchmarks. Among the pristine MoS$_x$ samples (Fig. S8a and b), MoS$_x$-hydro exhibits the highest activity (η_{10} = 187 mV; η_{100} = 312 mV), followed by amorphous MoS$_x$ (η_{10} = 240 mV; η_{100} = 340 mV), whereas MoS$_x$-800 shows the lowest activity (η_{10} = 314 mV; η_{100} = 439 mV). This trend correlates with the progressive decrease in exposed edge sites when transitioning from nanosheet-rich to basal-plane-dominated structures, highlighting the critical role of intrinsic active-site density in pristine MoS$_x$ catalysts. Upon Ni$_x$P modification, however, a pronounced reordering of the activity trend is observed. Notably, Ni$_x$P/MoS$_x$ requires overpotentials of only 96 and 170 mV to reach -10 and -100 mA cm^{-2}, respectively, outperforming all other heterostructures and approaching the performance of Pt/C at high current densities (Fig. 2a and b). This inversion of the intrinsic activity sequence indicates that interfacial electronic coupling, rather than morphology alone, governs HER performance. In contrast, Ni$_x$P/MoS$_x$-hydro exhibits only a

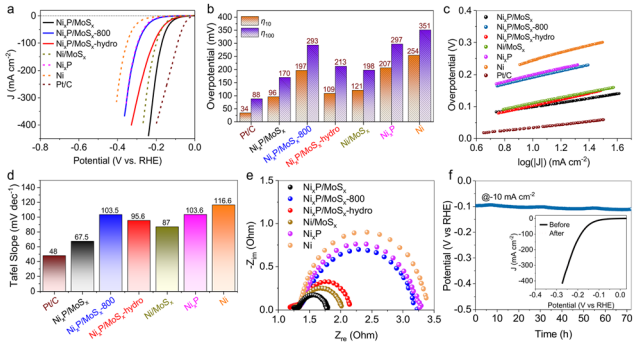

Fig. 2 (a) iR-corrected LSV curves measured in 1.0 M KOH, (b) corresponding overpotentials at −10 and −100 mA cm^{-2} (η_{10} and η_{100}), (c) Tafel plots and (d) extracted Tafel slopes for Ni_xP-modified MoS_x catalysts, together with Pt/C and control samples (Ni_xP, Ni and Ni/MoS_x) supported on carbon cloth. (e) EIS Nyquist plots for Ni_xP-modified MoS_x and control samples. (f) Chronopotentiometric stability test of Ni_xP/MoS_x at −10 mA cm^{-2} in 1.0 M KOH. Inset: LSV curves before and after the 72 h durability test.

moderate improvement (η_{10} = 109 mV; η_{100} = 213 mV), while Ni_xP/MoS_x-800 performs comparably to bare Ni_xP (Fig. 2a and b), suggesting a limited synergistic contribution of the highly crystalline MoS_2 support to the overall catalytic performance. Control experiments using Ni-only and Ni/MoS_x electrodes show significantly inferior activity (Fig. 2a and b), highlighting the critical role of phosphorus incorporation in modulating catalytic behavior. Furthermore, bare carbon cloth exhibits negligible activity (Fig. S8a), confirming that the observed catalytic response originates exclusively from the deposited active phases. Collectively, these results demonstrate that optimal HER performance is achieved at the amorphous–amorphous Ni_xP/MoS_x interface, emphasizing the importance of interfacial compatibility and strong electronic coupling. Notably, the performance of Ni_xP/MoS_x ranks among the highest reported for Ni–P-modified MoS_2-based electrocatalysts (Table S3).

Further mechanistic insight was obtained from Tafel analysis in the low-overpotential region, electrochemical impedance spectroscopy (EIS), and electrochemically active surface area (ECSA) measurements. Pristine MoS_x catalysts exhibit Tafel slopes of ∼98–136 mV dec^{-1} (Fig. S8c and d), consistent with Volmer-limited HER kinetics, where water dissociation constitutes the rate-determining step. Most Ni_xP- and Ni-modified samples retain similar behavior (Fig. 2c and d), including Ni_xP/MoS_x-800 (103.5 mV dec^{-1}), Ni_xP/MoS_x-hydro (95.6 mV dec^{-1}), as well as Ni_xP, Ni, and Ni/MoS_x control catalysts (∼87–116.6 mV dec^{-1}), indicating that the Volmer step remains kinetically limiting in these systems. In contrast, Ni_xP/MoS_x exhibits a markedly reduced Tafel slope of 67.5 mV dec^{-1}, indicative of a transition toward mixed Volmer–Heyrovsky kinetics with accelerated hydrogen evolution rates, approaching that of Pt/C (48 mV dec^{-1}). This kinetic shift suggests that the Ni_xP/MoS_x interface lowers the barrier for hydrogen adsorption and electrochemical desorption, thereby altering the rate-determining step. EIS measurements provide complementary evidence for this mechanistic evolution. Among pristine samples, MoS_x-hydro exhibits the lowest charge-transfer resistance (R_{ct}), as reflected by the smaller semicircle in Nyquist plots (Fig. S9), consistent with its superior intrinsic activity. Following Ni_xP deposition, however, Ni_xP/MoS_x displays the smallest semicircle diameter among all catalysts (Fig. 2e), corresponding to the lowest interfacial R_{ct} and most efficient charge transfer across the MoS_x/Ni_xP interface. In contrast, Ni_xP/MoS_x-hydro and Ni_xP/MoS_x-800 exhibit higher R_{ct}, while Ni_xP, Ni, and Ni/MoS_x control samples show significantly poorer charge-transfer characteristics. These results indicate that interfacial electronic coupling, rather than intrinsic conductivity alone, governs the charge-transfer kinetics in these heterostructures. ECSA analysis further reveals a clear decoupling between surface area and catalytic activity. For pristine MoS_x, the ECSA follows the trend: MoS_x-hydro (∼366 cm^2) > MoS_x (∼62 cm^2) > MoS_x-800 (∼29 cm^2), consistent with their HER activity (Fig. S10). However, this correlation breaks down upon Ni_xP modification (Fig. S11). Despite exhibiting the highest ECSA (∼551 cm^2), Ni_xP/MoS_x-hydro does not deliver the best performance. Instead, Ni_xP/MoS_x achieves the highest activity with a comparatively modest ECSA (∼75 cm^2), while the other samples with similar or larger surface areas (∼61–122 cm^2) remain less active. These findings demonstrate that HER activity is not governed by surface area alone but is instead dictated by interfacial charge-transfer kinetics. The amorphous Ni_xP/MoS_x interface uniquely optimizes hydrogen adsorption energetics and electron transfer, thereby overcoming the kinetic limitations associated with water dissociation.

The Ni_xP/MoS_x catalyst also exhibits excellent durability, retaining ∼87% of its initial activity after 72 h of continuous operation at −10 mA cm^{-2} (Fig. 2f). Notably, the catalyst maintains, and slightly improves, its HER performance upon reuse (η_{10} = 89 mV; η_{100} = 169 mV, Fig. 2f, inset), suggesting the formation of a stable and catalytically optimized interface under operating conditions. Post-catalysis characterization reveals no significant structural degradation but indicates limited surface reconstruction. XRD patterns remain unchanged (Fig. S12a), confirming preservation of the bulk phase, while Raman spectra show the emergence of weak Ni–O features (Fig. S12b), indicative of minor surface oxidation. EDS analysis reveals a shift in the Mo : S ratio toward the stoichiometric 1 : 2 value (Table S1), consistent with increased MoS_2-like ordering. XPS results (Fig. S13) confirm the predominance of Mo^{4+} species, along with partial oxidation of S and Ni. Importantly, the Ni : P ratio remains essentially unchanged (∼14 : 1; Table S1), indicating retention of the Ni–P phase during prolonged operation. Furthermore, in a two-electrode configuration, the integrated Ni_xP/MoS_x‖NiFe-LDH electrolyzer delivers low cell voltages of 1.46 and 1.61 V at 20 and 100 mA cm^{-2}, respectively (Fig. S14), demonstrating efficient overall water splitting and practical applicability under alkaline conditions.

To elucidate the origin of the enhanced catalytic activity, *operando* EIS combined with kinetic isotope effect (KIE) analysis was performed. Nyquist plots reveal a pronounced suppression of the high-frequency semicircle for Ni_xP/MoS_x relative to pristine MoS_x (Fig. 3a and b), indicating significantly reduced charge-transfer resistance and accelerated interfacial kinetics. Consistently, Bode phase analysis (Fig. 3c) shows faster surface

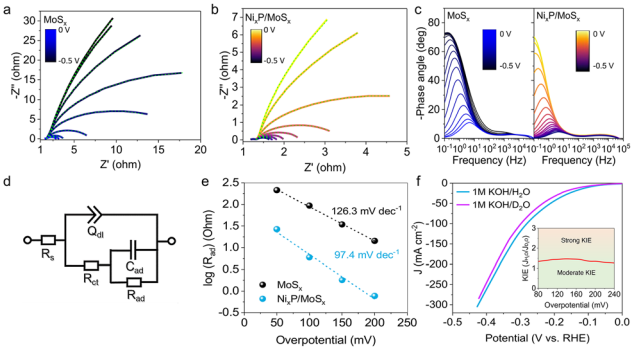

Fig. 3 *Operando* EIS Nyquist plots of (a) MoS_x and (b) Ni_xP/MoS_x recorded over a frequency range of 100 kHz to 0.1 Hz at applied potentials from 0 to −0.5 V *vs.* RHE (0.05 V increments). The dotted lines are fits to the data. (c) Corresponding *operando* Bode phase plots in 1.0 M KOH. (d) Armstrong–Henderson equivalent circuit model used for fitting the EIS data. (e) EIS-derived Tafel-like plots for MoS_x and Ni_xP/MoS_x. (f) LSV polarization curves of Ni_xP/MoS_x measured in 1.0 M KOH/H_2O and 1.0 M KOH/D_2O. Inset: The corresponding kinetic isotope effect (KIE), indicating a moderate isotope effect.

relaxation dynamics and more efficient charge dissipation for Ni_xP/MoS_x under increasing cathodic bias. Quantitative fitting using an Armstrong–Henderson equivalent circuit (Fig. 3d) confirms substantially lower R_{ct} values for Ni_xP/MoS_x compared to pristine MoS_x (Fig. S15a). Concurrently, an increase in the inverse adsorption resistance ($1/R_{ad}$) and adsorption pseudocapacitance (C_{ad}) is observed (Fig. S15b and c), reflecting accelerated hydrogen adsorption/desorption kinetics and increased surface coverage of H* intermediates.[43,44] All extracted fitting parameters are summarized in Table S4. EIS-derived Tafel analysis ($\log(R_{ad})$ *vs.* η)[45] yields a reduced slope for Ni_xP/MoS_x ($\sim$97 mV dec^{-1}) compared to pristine MoS_x ($\sim$126 mV dec^{-1}) (Fig. 3e), indicating facilitated proton-electron transfer and a deviation from purely Volmer-limited behavior. This interpretation is further supported by KIE measurements (Fig. 3f), which show moderate J_{H_2O}/J_{D_2O} values ($\sim$1.2–1.5) near the HER onset. These values are consistent with a quasi-equilibrated Volmer step, suggesting that water dissociation is no longer the sole rate-determining step. Collectively, the *operando* EIS and KIE analyses demonstrate that Ni_xP modification effectively alleviates the kinetic bottleneck associated with water dissociation, promoting a transition from a Volmer-limited pathway to post-Volmer kinetics governed by accelerated hydrogen adsorption/desorption dynamics. This synergistic enhancement of charge-transfer and surface reaction kinetics provides a mechanistic basis for the observed activity improvement and explains the inversion of the conventional morphology–activity relationship.

In summary, Ni_xP surface modification fundamentally reshapes the activity landscape of MoS_x electrocatalysts *via* morphology-dependent interfacial coupling. Although polycrystalline MoS_x nanosheets show higher intrinsic activity, Ni_xP incorporation reverses this trend, rendering the amorphous–amorphous Ni_xP/MoS_x interface the most active (η_{10} = 96 mV, Tafel slope = 67.5 mV dec^{-1}). *Operando* electrochemical measurements and kinetic isotope effect analysis reveal that interfacial electronic coupling enhances charge-transfer efficiency and hydrogen adsorption kinetics, enabling a transition beyond a Volmer-limited mechanism. The Ni_xP/MoS_x catalyst also exhibits excellent durability and efficient overall water splitting (1.46 V at 20 mA cm^{-2}), highlighting the critical role of amorphous interfaces in catalyst design.

I. Vamvasakis: data curation, methodology and analysis, writing of the original draft; A. Grammenos: investigation, synthesis, characterization, writing; G. S. Armatas: funding acquisition, conceptualization, general supervision, writing, review and editing.

Conflicts of interest

There are no conflicts to declare.

Data availability

The data supporting the findings of this study are available within the article and its supplementary information (SI). Supplementary information: detailed experimental methods, synthetic procedures, and catalytic and spectroscopic characterization data. See DOI: https://doi.org/10.1039/d6cc01893a.

Acknowledgements

This study was carried out within the framework of the National Recovery and Resilience Plan Greece 2.0 (Award No. TAEDR-0535821), funded by the European Union – NextGenerationEU. The open access publishing of this article is financially supported by HEAL-Link.

References

1 G. Squadrito, G. Maggio and A. Nicita, *Renewable Energy*, 2023, **216**, 119041.
2 W. Sheng, H. A. Gasteiger and Y. Shao-Horn, *J. Electrochem. Soc.*, 2010, **157**, B1529.
3 W. Sheng, M. Myint, J. G. Chen and Y. Yan, *Energy Environ. Sci.*, 2013, **6**, 1509–1512.
4 J. Durst, A. Siebel, C. Simon, F. Hasché, J. Herranz and H. A. Gasteiger, *Energy Environ. Sci.*, 2014, **7**, 2255–2260.
5 N. Mahmood, Y. Yao, J. W. Zhang, L. Pan, X. Zhang and J. J. Zou, *Adv. Sci.*, 2018, **5**, 1700464.
6 M. Zeng and Y. Li, *J. Mater. Chem. A*, 2015, **3**, 14942–14962.
7 X. Zou and Y. Zhang, *Chem. Soc. Rev.*, 2015, **44**, 5148–5180.
8 B. Hinnemann, P. G. Moses, J. Bonde, K. P. Jørgensen, J. H. Nielsen, S. Horch, I. Chorkendorff and J. K. Nørskov, *J. Am. Chem. Soc.*, 2005, **127**, 5308–5309.
9 D. Merki, S. Fierro, H. Vrubel and X. Hu, *Chem. Sci.*, 2011, **2**, 1262–1267.
10 R. J. Toh, Z. Sofer, J. Luxa, D. Sedmidubský and M. Pumera, *Chem. Commun.*, 2017, **53**, 3054–3057.
11 M. D. Patel, J. Zhang, J. Park, N. Choudhary, J. M. Tour and W. Choi, *Mater. Lett.*, 2018, **225**, 65–68.
12 Q. Zhou, X. Luo, Y. Li, Y. Nan, H. Deng, E. Ou and W. Xu, *Int. J. Hydrogen Energy*, 2020, **45**, 433–442.
13 C. Niu, H. Song, Y. Chang, W. Hou, Y. Li, Y. Zhao, Y. Xiao and G. Han, *J. Alloys Compd.*, 2022, **900**, 163509.
14 Y. Li, Y. Yu, Y. Huang, R. A. Nielsen, W. A. Goddard, Y. Li and L. Cao, *ACS Catal.*, 2014, **5**, 448–455.
15 T. F. Jaramillo, K. P. Jørgensen, J. Bonde, J. H. Nielsen, S. Horch and I. Chorkendorff, *Science*, 2007, **317**, 100–102.
16 J. Kibsgaard, Z. Chen, B. N. Reinecke and T. F. Jaramillo, *Nat. Mater.*, 2012, **11**, 963–969.

17 E. D. Koutsouroubi, I. Vamvasakis, M. G. Minotaki, I. T. Papadas, C. Drivas, S. A. Choulis, G. Kopidakis, S. Kennou and G. S. Armatas, *Appl. Catal., B*, 2021, **297**, 120419.
18 F. Zakerian, M. Fathipour, R. Faez and G. Darvish, *J. Theor. Appl. Phys.*, 2019, **13**, 55–62.
19 Y. Zhou, C. Li, Y. Zhang, L. Wang, X. Fan, L. Zou, Z. Cai, J. Jiang, S. Zhou, B. Zhang, H. Zhang, W. Li and Z. Chen, *Adv. Funct. Mater.*, 2023, **33**, 2304302.
20 P. Man, S. Jiang, K. H. Leung, K. H. Lai, Z. Guang, H. Chen, L. Huang, T. Chen, S. Gao, Y. K. Peng, C. S. Lee, Q. Deng, J. Zhao and T. H. Ly, *Adv. Mater.*, 2024, **36**, 2304808.
21 X. Zhang and Y. Liang, *Adv. Sci.*, 2018, **5**, 1700644.
22 M. Kim, M. A. R. Anjum, M. Lee, B. J. Lee and J. S. Lee, *Adv. Funct. Mater.*, 2019, **29**, 1809151.
23 M. S. Metaxa, I. Vamvasakis, G. Kopidakis, G. Kioseoglou and G. S. Armatas, *Chem. Eng. J.*, 2025, **525**, 170118.
24 M. S. Metaxa, I. Vamvasakis and G. S. Armatas, *Small*, 2025, **22**, e13136.
25 M. S. Metaxa, I. Vamvasakis and G. S. Armatas, *Energy Environ. Mater.*, 2026, **9**, e70187.
26 P. Liu and J. A. Rodriguez, *J. Am. Chem. Soc.*, 2005, **127**, 14871–14878.
27 E. J. Popczun, J. R. McKone, C. G. Read, A. J. Biacchi, A. M. Wiltrout, N. S. Lewis and R. E. Schaak, *J. Am. Chem. Soc.*, 2013, **135**, 9267–9270.
28 S. Bra, I. Vamvasakis, E. K. Andreou, G. Vailakis, G. Kopidakis and G. S. Armatas, *Int. J. Hydrogen Energy*, 2023, **48**, 25300–25314.
29 N. Jiang, B. You, M. Sheng and Y. Sun, *ChemCatChem*, 2016, **8**, 106–112.
30 D. H. Song, D. Hong, Y. K. Kwon, H. W. Kim, J. Shin, J. Shin, H. M. Lee and E. A. Cho, *J. Mater. Chem. A*, 2020, **8**, 12069–12079.
31 A. B. Silva, M. Medina, L. A. Goulart and L. H. Mascaro, *Electrochim. Acta*, 2024, **475**, 143679.
32 G. Q. Han, X. Li, J. Xue, B. Dong, X. Shang, W. H. Hu, Y. R. Liu, J. Q. Chi, K. L. Yan, Y. M. Chai and C. G. Liu, *Int. J. Hydrogen Energy*, 2017, **42**, 2952–2960.
33 S. Hu, Q. Cao, H. Yao, Y. Jia and X. Guo, *ChemCatChem*, 2024, **16**, e202301420.
34 E. A. Ponomarev, M. Neumann-Spallart, G. Hodes and C. Lévy-Clément, *Thin Solid Films*, 1996, **280**, 86–89.
35 S. Subramaniyam, S. Bharatan, S. Muthusamy and S. Sivaprakasam, *Coatings*, 2025, **15**, 146.
36 K. Gołasa, M. Grzeszczyk, R. Bozek, P. Leszczyński, A. Wysmołek, M. Potemski and A. Babiński, *Solid State Commun.*, 2014, **197**, 53–56.
37 Z. Bojarska, M. Mężydło, M. Mazurkiewicz-Pawlicka and Ł. Makowski, *Appl. Sci.*, 2022, **12**, 11293.
38 N. Moses Badlyan, N. Pettinger, N. Enderlein, R. Gillen, X. Chen, W. Zhang, K. C. Knirsch, A. Hirsch and J. Maultzsch, *Phys. Rev. B*, 2022, **106**, 104103.
39 M. Chen, D. Liu, Y. Chen, D. Liu, X. Du, J. Feng, P. Zhou, B. Zi, Q. Liu, K. H. Lo, S. Chen, S. Wang, W. F. Ip and H. Pan, *Appl. Mater. Today*, 2022, **26**, 101343.
40 M. Moloudi, A. Noori, M. S. Rahmanifar, M. F. El-Kady, E. Mousali, N. B. Mohamed, X. Xia, Y. Zhang, A. Vinu, M. Vincent, D. Kowalski, R. B. Kaner and M. F. Mousavi, *Chem. Sci.*, 2025, **16**, 9484–9500.
41 C. H. Lee, J. M. Yun, S. Lee, S. M. Jo, K. Eom, D. C. Lee, H. I. Joh and T. F. Fuller, *Sci. Rep.*, 2017, **7**, 41190.
42 J. Kibsgaard, T. F. Jaramillo and F. Besenbacher, *Nat. Chem.*, 2014, **6**, 248–253.
43 N. Krstajić, M. Popović, B. Grgur, M. Vojnović and D. Šepa, *J. Electroanal. Chem.*, 2001, **512**, 16–26.
44 E. A. Franceschini, G. I. Lacconi and H. R. Corti, *Electrochim. Acta*, 2015, **159**, 210–218.
45 Y. Zhu, M. Klingenhof, C. Gao, T. Koketsu, G. Weiser, Y. Pi, S. Liu, L. Sui, J. Hou, J. Li, H. Jiang, L. Xu, W. H. Huang, C. W. Pao, M. Yang, Z. Hu, P. Strasser and J. Ma, *Nat. Commun.*, 2024, **15**, 1447.